



Contents lists available at ScienceDirect

# Journal of Quantitative Spectroscopy & Radiative Transfer

journal homepage: [www.elsevier.com/locate/jqsrt](http://www.elsevier.com/locate/jqsrt)

## An algorithm for hyperspectral remote sensing of aerosols: 1. Development of theoretical framework

Weizhen Hou<sup>a</sup>, Jun Wang<sup>a,\*</sup>, Xiaoguang Xu<sup>a</sup>, Jeffrey S. Reid<sup>b</sup>, Dong Han<sup>a</sup><sup>a</sup> Earth and Atmospheric Sciences, University of Nebraska–Lincoln, 303 Bessey Hall, Lincoln, NE 68588, USA<sup>b</sup> Marine Meteorology Division, Naval Research Laboratory, 7 Grace Hopper Ave, Stop 2, Monterey, CA 93943, USA

### ARTICLE INFO

#### Article history:

Received 20 November 2015

Received in revised form

12 January 2016

Accepted 12 January 2016

Available online 21 January 2016

#### Keywords:

GEO-TASO

TEMPO

Principal Component Analysis (PCA)

Hyperspectral Remote Sensing

Aerosol Retrieval

Surface Reflectance Reconstruction

### ABSTRACT

This paper describes the first part of a series of investigations to develop algorithms for *simultaneous* retrieval of aerosol parameters and surface reflectance from a newly developed hyperspectral instrument, the GEOstationary Trace gas and Aerosol Sensor Optimization (GEO-TASO), by taking full advantage of available hyperspectral measurement information in the visible bands. We describe the theoretical framework of an inversion algorithm for the hyperspectral remote sensing of the aerosol optical properties, in which major principal components (PCs) for surface reflectance is assumed known, and the spectrally dependent aerosol refractive indices are assumed to follow a power-law approximation with four unknown parameters (two for real and two for imaginary part of refractive index). New capabilities for computing the Jacobians of four Stokes parameters of reflected solar radiation at the top of the atmosphere with respect to these unknown aerosol parameters and the weighting coefficients for each PC of surface reflectance are added into the UNified Linearized Vector Radiative Transfer Model (UNL-VRM), which in turn facilitates the optimization in the inversion process. Theoretical derivations of the formulas for these new capabilities are provided, and the analytical solutions of Jacobians are validated against the finite-difference calculations with relative error less than 0.2%. Finally, self-consistency check of the inversion algorithm is conducted for the idealized green-vegetation and rangeland surfaces that were spectrally characterized by the U.S. Geological Survey digital spectral library. It shows that the first six PCs can yield the reconstruction of spectral surface reflectance with errors less than 1%. Assuming that aerosol properties can be accurately characterized, the inversion yields a retrieval of hyperspectral surface reflectance with an uncertainty of 2% (and root-mean-square error of less than 0.003), which suggests self-consistency in the inversion framework. The next step of using this framework to study the aerosol information content in GEO-TASO measurements is also discussed.

© 2016 Elsevier Ltd. All rights reserved.

### 1. Introduction

The global distribution of atmospheric aerosol properties has been retrieved routinely from different satellite remote sensing instruments that vary in spectral range,

spectral resolution, angular range, polarization capability, spatial resolution, etc. [1,2]. These instruments (with acronyms expanded in Table 1) generally can be divided in the two categories: (1) imager or radiometer that measures intensity (and sometimes polarization) at multi-wavelength with a single view direction such as the AVHRR [3,4], MERIS [5], and the MODIS [6–9], or with multiple view angles such as AASTR [10,11], MISR [12,13], and POLDER [14–16]; (2) spectrometer that measures

\* Corresponding author. Tel.: +1 402 472 3597.

E-mail address: [jwang7@unl.edu](mailto:jwang7@unl.edu) (J. Wang).

**Table 1**  
List of current/future typical multispectral/hyperspectral space-borne sensors.

Senor acronym	Full name	Spectral range ( $\mu\text{m}$ )	Spectral resolution (nm)	Band number
AVHRR/2	Advanced Very High Resolution Radiometer	0.58–12.40	100–1000	5
AVHRR/3		0.58–12.50		6
MERIS	MEDium Resolution Imaging Spectroradiometer	0.41–0.90	7.5–200	15
MODIS	MODerate resolution Imaging Spectroradiometer	0.40–14.39	10–500	36
AATSR	Advanced Along Track Scanning Radiometer	0.55–12.00	20–40	7
MISR	Multi-angle Imaging SpectroRadiometer	0.44–0.87	22–42	4
POLDER	POLarization and Directionality of the Earth's Reflectances	0.44–0.91	10–40	9
Hyperion	Hyperion imaging spectrometer	0.40–2.50	10	220
GOME-2	Global Ozone Monitoring Experiment	0.24–0.79	0.2–0.4	–
SCIAMACHY	SCanning Imaging Absorption spectroMeter for Atmospheric CHartography	0.24–1.70	0.2–1.5	–
OMI	Ozone Monitoring Instrument	0.27–0.50	0.45–1.0	–
AIRS	Atmospheric InfraRed Sounder	0.41–0.94	30–450	4
		3.70–15.40	–	2378
IASI	Infrared Atmospheric Sounding Interferometer	3.62–15.50	0.5 $\text{cm}^{-1}$	8461
GEMS	Geostationary Environmental Monitoring Spectrometer	0.30–0.50	0.6	–

AIRS has a hyperspectral spectrometer in the thermal infrared band and a multi-spectral photometer in the visible/near-infrared band.

intensity at hyperspectral resolution, such as Hyperion [17], GOME-2 [18–21], SCIAMACHY [22,23], OMI [24,25], AIRS [26,27] and IASI [28,29]. Correspondingly, two categories of inversion algorithms exist: one focuses on the use of several atmospheric window channels (such as those from MODIS or MISR) to retrieve fine/coarse mode aerosol optical depth (AOD) [30], and another focuses on the use of hyperspectral data (generally more than 10 channels) to retrieve AOD as well as other information [31].

This paper presents findings for the first part of a series of studies that aim to develop a hyperspectral remote sensing technique for retrieving aerosol properties from a newly developed GEOstationary Trace gas and Aerosol Sensor Optimization (GEO-TASO) instrument. GEO-TASO measures the radiance at spectral resolution of 0.28 nm in the spectral range of 400–700 nm. GEO-TASO instrument is a prototype instrument of Tropospheric Emissions: Monitoring of POLLution (TEMPO) that is scheduled to be launched before 2022 to measure aerosol particles, ozone, and other selected trace gases from a geostationary orbit over the North America [32]. TEMPO is part of future geosatellite constellation that also includes GEMS (Table 1) from Korea [33], and Sentinel-4 from Europe [34], and together they will provide hyperspectral measurements in the visible spectral range almost globally and hourly over the sunlit areas.

Past inversion algorithms for hyperspectral remote sensing of aerosols primarily use the radiance data collected at thermal infrared wavelengths, including those using AIRS and IASI to retrieve coarse aerosol properties such as dust AOD and particle size distribution (PSD) from satellites [35]. Yet, the properties of fine aerosol particles in visible and near infrared cannot be well quantified from measurements in the thermal infrared spectrum, for the reason that the infrared and visible spectra are not sensitive to the same ranges of particle sizes [35], and the radiative extinction of fine-mode aerosols decrease rapidly from the visible to the infrared spectrum. Nevertheless, if fine-mode aerosols have distinct absorption features in the infrared, some information such as the spatial coverage of

sulfuric acid with absorption in IASI can still be inferred from infrared data [31].

Since TEMPO and several future geostationary satellites will take measurements in the ultraviolet (UV) and visible spectra at a high spectral resolution, the question arises: can more aerosol information (in addition to optical depth) be retrieved over land by using such measurements? In the past, such measurements are primarily used to derive surface properties after atmospheric correction [36]. The atmospheric correction algorithms for hyperspectral images are usually based on the radiative transfer (RT) modeling methods, such as 6S [37,38] and MODTRAN [39], and thus there are various software available to model the atmosphere mainly containing ATREM [40], ATCOR [41], FLAASH [42,43], ACORN [44] and HATCH [45], for which the detailed descriptions and references are shown in Table 2. A differential absorption method is usually used to estimate water vapor column for atmospheric correction in near-infrared bands [46,47]. As for the aerosol information, AOD is often derived from in situ data or the visibility data in the atmospheric correction algorithm for hyperspectral measurements. Meanwhile, algorithms focusing on aerosol retrievals have also been designed and developed. Regardless of the algorithms for atmospheric correction or surface characterization, the problem is to decouple atmospheric information from surface, and decide what parameters to be retrieved (and/or assumed) for surface and for atmosphere, respectively. Since measurement at one wavelength can only be used to retrieve one piece of information, assumption needs to be made about surface properties or aerosol properties. In the past, surface properties are either prescribed such as in deep blue algorithm for MODIS [6,7], or are derived by a dark pixel reflectance ratio (0.66  $\mu\text{m}$  and 2.1  $\mu\text{m}$ ) method based on work of Kaufman et al. [48] and Levy et al. [8].

To take full advantage of the hyperspectral information, some assumptions for surface reflectance need to be given. Generally, the surface reflectance in hyperspectral resolution can be regarded as a mixture of different surface reflectance spectra corresponding to such features of specific plant canopy and soil characteristics of the surface.

**Table 2**

List of software programs for hyperspectral atmospheric correction.

Acronym	Full name
ATREM	ATmospheric REMoval algorithm
ATCOR	ATmospheric CORrection
FLAASH	Fast Line-of-sight Atmospheric Analysis of Spectral Hypercubes
ACORN	Atmospheric CORrection Now
HATCH	High accuracy ATmospheric Correction for Hyperspectral data
6S	Second Simulation of the Satellite Signal in the Solar Spectrum
MODTRAN	MODerate resolution atmospheric TRANsmission

Hence, the principal components analysis (PCA) techniques [49] has been widely used in the land surface and atmospheric remote sensing to classify different plant function types [50,51], identify the chemical elements and minerals in rocks [52], and to conduct the spectral compression for hyperspectral feature extraction [53,54], as well as infrared radiative transfer calculation [55–58]. Thus, there is a history of deconvolving surface reflectance at hyperspectral resolution into various components, with each component corresponding to the unique spectral characteristics of each surface elements (such as different types of plants and soils), and with weighting coefficients for each component intrinsically linked to the area and layout of these elements [59]. With this assumption, the surface reflectance can be characterized by the weighting coefficients for each spectral principal component (PC); normally only a few PCs are needed to describe the surface reflectance with high accuracy, provided the PCs are known. For example, Bell and Baranoski [60] used 12–20 PCs to describe surface reflectance of plant from 400 nm to 2500 nm with different error tolerances.

Encouraged by the previous work described above, we developed a theoretical framework for conducting the hyperspectral remote sensing of aerosol particles in the visible bands with optimal estimation (OE) approach [61,62], under the assumption that the PCs for surface hyperspectral reflectance can be pre-described. The basis for this assumption is that: (a) we have knowledge of land surface types globally at 500 m  $\times$  500 m resolution such as from MODIS land surface type data and surface reflectance data [63]; (b) there are several spectral libraries that describe the reflectance at hyperspectral resolution for the same surface type but sampled at different ambient conditions (e.g., grass sampled in different time in the growing season), such as ASTER spectral library [64] and U.S. Geological Survey (USGS) digital spectral library [65]. With (a) and (b), the PCs of reflectance can be available at 1 km<sup>2</sup> resolution at least over the areas covered by green canopy (if not globally). Hence, instead of making assumption (of aerosol properties) for retrieving surface reflectance or making assumption (of surface properties) for retrieving aerosol properties *separately*, our retrieval framework aims to retrieve the aerosol optical properties and the weighting coefficients for each surface reflectance PCs (and therefore surface reflectance) *simultaneously*.

In addition to the joint retrieval of aerosol and surface reflectance, our method has two other retrieval strategies that differ from the past studies include:

- (1) We use OE method for the inversion instead of the look-up table approach that is used in many existing operational aerosol algorithms. The OE method is needed because the number of spectral bands of hyperspectral observations is much higher than those of multi-spectral instruments, and hence, it is not feasible to create a look-up table of hyperspectral top-of-atmosphere (TOA) reflectance as a function of wavelength, viewing geometries and wavelength-dependent aerosol properties.
- (2) The effective radius and effective variance are used to represent a bi-modal lognormal size distribution for fine and coarse mode respectively; meanwhile, the relationship of the refractive index with respect to the wavelength are parameterized with less number of unknown parameters, thus the hyperspectral retrieval approach could be significant simplified.

To implement these new retrieval strategies in the spectral reflectance fitting requires the use of a radiative transfer model to serve as a forward model that can compute not only the TOA reflectance but also the sensitivity (or Jacobians) of the reflectance with respect to (*w.r.t.*) the retrieval [66]. For this purpose, we select the UNified Linearized Vector Radiative Transfer Model (UNL-VRM) as the forward model [66–68].

As the first part of a series of studies, this paper focuses on the development and implementation of the retrieval framework articulated above. Applying this framework for the information content analysis to explore the feasibility to retrieve the particle size distribution and wavelength-dependence of refractive index, as well as to conduct retrievals with real GEO-TASO data will be presented in future studies. We provide in Section 2 a brief description of UNL-VRM including the recent new development that enables the calculation of Jacobians of reflectance with respect to the weighting coefficients of each PC of surface reflectance and the parameters that describe the aerosol-wavelength dependence. Numerical experiments that were designed to conduct self-consistency checks of the retrieval algorithm are described in Section 3 for two land surface types: green vegetation and rangeland surfaces. The results are presented and discussed in Section 4. Finally, Section 5 provides the summary and conclusion.

## 2. Model and algorithm developments

The flowchart of newly developed inversion algorithm based on surface PCs is presented in Fig. 1. The forward model, UNL-VRM, integrates five modules for the calculation of aerosol single scattering, gas absorption and radiative transfer [66]. These five modules include a linearized vector radiative transfer model VLIDORT [69], a linearized Mie and T-matrix scattering code [70], a surface bidirectional reflectance distribution function (BRDF) module, and a module for line-by-line calculation of

Rayleigh scattering and gas absorption. Inputs for the UNL-VRM contain profiles of atmospheric properties and constituents, such as temperature, pressure, aerosol mass concentration or layer AOD, water vapor amount and other trace gas volume mixing ratio profiles, as well as the aerosol parameters themselves, including particle size distribution and refractive index. The outputs of UNL-VRM include not only 4 elements of the Stokes vector  $\mathbf{I} = [I, Q, U, V]^T$ , but also contain their sensitivities (Jacobians) with respect to the aerosol properties (including scattering properties, size, and refractive index) and surface reflectance parameters (in BRDF). In addition, two modules for the analysis, including an optimal inversion code and a visualization tool for diagnosis, are also integrated in UNL-VRM. UNL-VRM has also been used to study the information content of aerosol particles in the ground-based measurements of multispectral radiance and polarization of sky light [67], and develop algorithm for retrieval of fine-mode and coarse-mode aerosol

refractive index and particle size distribution parameters from such measurements taken in Beijing [68].

### 2.1. Jacobians of TOA reflectance w.r.t. surface reflectance PCs

Our hyperspectral retrieval technique assumes that, for a given location, the surface reflectance can be decomposed into several PCs with different weighting coefficients, and we have a good knowledge of these PCs (such as for vegetated surfaces). For a given specific location, atmospheric aerosol particles can highly vary within a couple of hours or days, while the change of surface properties are relatively small. Indeed, MODIS land surface algorithm for BRDF retrievals assumes that surface properties for a given location are relatively constant within 16 days [63]. A similar assumption is made for the Multi-Angle Implementation of Atmospheric Correction (MAIAC) algorithm [71]. Furthermore, the surface reflectance depends on the type of canopy or plants over the soil surface, the soil characteristics, and so on. Hence, the surface reflectance in hyperspectral resolution can show a combined effect of many local features in that surface [72]. For example, the reflectance of green vegetated surfaces will have a peak in the green band, while reflectance of dry vegetation and bare soil will increase with wavelength in the visible bands, just as some spectral curves of typical land surface type shown in Fig. 2. Among those spectral curves, rangeland has a mixture surface type, including the grassland, shrub land, woodland, wetland and deserts that are grazed by domestic livestock or wild animals.

With the assumption that we know surface reflectance PCs, the retrieval algorithm needs to retrieve the weighting coefficients of these components as well as spectral-dependent aerosol properties simultaneously at the same time. To this end, we develop the new capabilities in UNL-VRM that can compute the sensitivity of TOA-reflectance with respect to the weighting coefficients of each PC of surface reflectance.

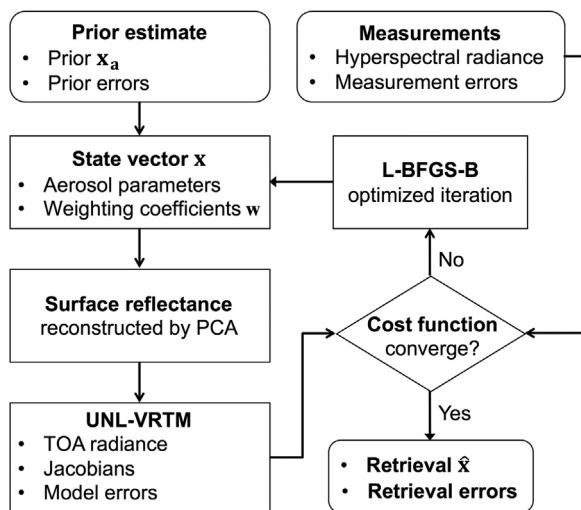


Fig. 1. Flowchart of the PCA-based inversion algorithm.

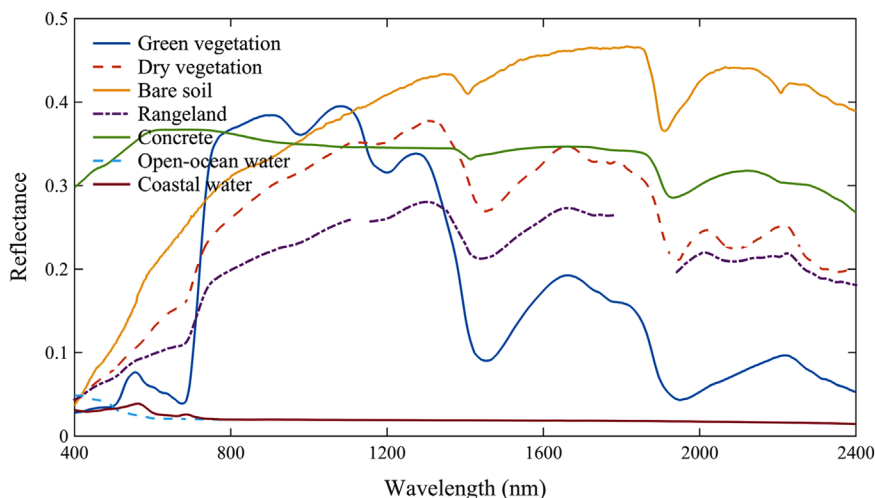


Fig. 2. Spectral reflectances for different land surfaces, in which the spectra of bare soil are selected from the ASTER spectral library, other spectra are selected from the USGS spectral library.

Suppose we have a spectral reflectance dataset for  $n_s$  samples of the same surface type (such as vegetation), and for each sample, the reflectance is measured at  $d$  number of wavelengths. Following the procedure of PCA [73], the surface reflectance at each band for a given sample could be represented and reconstructed by the PCs as

$$\mathbf{r} = \mathbf{P}\mathbf{w}, \quad (1)$$

where  $\mathbf{r}$  means the vector of surface reflectance spectra,  $\mathbf{P}$  is the matrix that constituted by each PC as the column vector, and  $\mathbf{w}$  represents the weighting coefficients vector corresponding to the PCs. If only the first  $m$  PCs are considered, Eq. (1) can be written as

$$\begin{bmatrix} r_{\lambda_1} \\ \vdots \\ r_{\lambda_d} \end{bmatrix} = \begin{bmatrix} P_{1,1} & \cdots & P_{1,m} \\ \vdots & \ddots & \vdots \\ P_{d,1} & \cdots & P_{d,m} \end{bmatrix} \begin{bmatrix} w_1 \\ \vdots \\ w_m \end{bmatrix}, \quad (2)$$

here  $r_{\lambda_i}$  denotes the surface reflectance at the wavelength  $\lambda_i$ , ( $i = 1, \dots, d$ ) and the subscript  $i$  represents index for the  $i$ th wavelength, and the PC weighting coefficients vector  $\mathbf{w} = [w_1, \dots, w_m]^T$ , ( $m \leq d$ ), here the superscript  $T$  represents the transpose operation.

Following the relationship of Eqs. (1) and (2), the weighting coefficients vector  $\mathbf{w}$  could be solved as a least square solution:

$$\mathbf{w} = \mathbf{P}^+ \mathbf{r}, \quad (3)$$

where the pseudo-inverse  $\mathbf{P}^+$  means a generalized inverse matrix of matrix  $\mathbf{P}$  [74]. Because  $\mathbf{P}$  is orthogonalized in column and has full column rank, matrix  $\mathbf{P}^* \mathbf{P}$  is invertible. Consequently, the Moore-Penrose pseudo-inverse matrix  $\mathbf{P}^+$  can be expressed in a simple algebraic formula as

$$\mathbf{P}^+ = (\mathbf{P}^* \mathbf{P})^{-1} \mathbf{P}^*, \quad (4)$$

here  $\mathbf{P}^*$  denotes Hermitian transpose (also called conjugate Transpose) matrix [75]. Therefore, the weighting coefficients vector  $\mathbf{w}$  could be computed and the spectra of surface reflectance could be reconstructed.

In order to the get the Jacobian results of the TOA radiance *w.r.t.* weighting coefficients vector  $\mathbf{w}$ , following the relationship in Eq. (2), the Jacobian vector can be written as

$$\frac{\partial I}{\partial \mathbf{w}} = \frac{\partial I}{\partial r_{\lambda_i}} \frac{\partial r_{\lambda_i}}{\partial \mathbf{w}}, \quad (i = 1, \dots, d), \quad (5)$$

where the  $I$  means the TOA radiance normalized to the spectral solar irradiance, hereafter we call it radiance (no unit), and the subscript  $\lambda$  has been omitted for simplification. Due to

$$\frac{\partial r_{\lambda_i}}{\partial \mathbf{w}} = \left[ \frac{\partial r_{\lambda_i}}{\partial w_1}, \frac{\partial r_{\lambda_i}}{\partial w_2}, \dots, \frac{\partial r_{\lambda_i}}{\partial w_m} \right]^T = [P_{i,1}, P_{i,2}, \dots, P_{i,m}]^T, \quad (i = 1, \dots, d), \quad (6)$$

we have:

$$\frac{\partial I}{\partial \mathbf{w}} = \frac{\partial I}{\partial r_{\lambda_i}} [P_{i,1}, P_{i,2}, \dots, P_{i,m}]^T, \quad (i = 1, \dots, d). \quad (7)$$

Since the first term on the right hand side of Eq. (7) is readily available in UNL-VRM for a Lambertian surface, Eq. (5) is implemented as part of the new development of UNL-VRM.

While Eq. (5) is valid for a specific geometry, the kernel-driven BRDF model for surface reflectance in UNL-VRM can be presented as

$$r_{\lambda}(\theta_0, \theta_v, \phi) = f_{\text{iso}}(\lambda) + k_1(\lambda) f_{\text{geom}}(\theta_0, \theta_v, \phi) + k_2(\lambda) f_{\text{vol}}(\theta_0, \theta_v, \phi), \quad (8)$$

where  $f_{\text{iso}}$ ,  $f_{\text{geom}}$ ,  $f_{\text{vol}}$  respectively represent isotropic, geometric-optical and volumetric surface scattering [76,77],  $\theta_0$ ,  $\theta_v$ ,  $\phi$  are the observation geometries, respectively represent the sun zenith angle, viewing zenith angle and relative azimuth angle, and  $f_{\text{iso}}(\lambda)$ ,  $k_1(\lambda)$ ,  $k_2(\lambda)$  are the coefficients of the BRDF kernels at the wavelength  $\lambda$ . Correspondingly, the Jacobian results including  $\frac{\partial I}{\partial f_{\text{iso}}(\lambda)}$ ,  $\frac{\partial I}{\partial k_1(\lambda)}$ ,  $\frac{\partial I}{\partial k_2(\lambda)}$  that is already part of UNL-VRM [69] can be used to compute the first term on the right-hand side of Eq. (5):

$$\frac{\partial I}{\partial r_{\lambda}} = \frac{\left[ f_{\text{iso}}(\lambda) \frac{\partial I}{\partial f_{\text{iso}}(\lambda)} + k_1(\lambda) \frac{\partial I}{\partial k_1(\lambda)} + k_2(\lambda) \frac{\partial I}{\partial k_2(\lambda)} \right]}{r_{\lambda}}, \quad (9)$$

in which the subscript of variable  $\lambda$  of  $I$  has been omitted in the above expression. Combining Eq. (7) and Eq. (9), the results of  $\frac{\partial I}{\partial \mathbf{w}}$  for BRDF case could be calculated.

For the practical simulation of hyperspectral data, the three coefficients in Eq. (8) vary with the wavelength, and their values should be given at each wavelength in the input file of UNL-VRM. To make the work for input parameters easier and simpler, we follow the way of rewritten formulas in the work of Litvinov et al. [78] as

$$r_{\lambda}(\theta_0, \theta_v, \phi) = k(\lambda) \left[ 1 + k_1 f_{\text{geom}}(\theta_0, \theta_v, \phi) + k_2 f_{\text{vol}}(\theta_0, \theta_v, \phi) \right] \quad (10)$$

where  $k_1 = 0.087$ ,  $k_2 = 0.688$  for vegetation surface, and  $k(\lambda)$  can be obtained by using the Lambertian surface reflectance from the vegetation dataset.

## 2.2. Assumptions on the wavelength-dependent refractive index

Since it is not possible to retrieve the complex index of refraction at all wavelengths at the same time, we simplify its dependence on the wavelength following the assumption by Dubovik and King [79] and assume that the variations of real part and imaginary of refractive index as a function of wavelength satisfy the relationship:

$$\begin{cases} m_r(\lambda) = m_r(\lambda_0) \left( \frac{\lambda}{\lambda_0} \right)^{-b_r} = m_{r,0} \cdot \left( \frac{\lambda}{\lambda_0} \right)^{-b_r} \\ m_i(\lambda) = m_i(\lambda_0) \left( \frac{\lambda}{\lambda_0} \right)^{-b_i} = m_{i,0} \cdot \left( \frac{\lambda}{\lambda_0} \right)^{-b_i} \end{cases} \quad (11)$$

where  $m_{r,0}$ ,  $b_r$ ,  $m_{i,0}$  and  $b_i$  are the coefficients,  $\lambda$  represents the wavelength and  $\lambda_0$  is the wavelength of reference. Thus, the Jacobians expression for the real part could be written as

$$\begin{cases} \frac{\partial I}{\partial m_{r,0}} = \frac{\partial I}{\partial m_r(\lambda)} \frac{\partial m_r(\lambda)}{\partial m_{r,0}} = \left( \frac{\lambda}{\lambda_0} \right)^{-b_r} \frac{\partial I}{\partial m_r(\lambda)} \\ \frac{\partial I}{\partial b_r} = \frac{\partial I}{\partial m_r(\lambda)} \frac{\partial m_r(\lambda)}{\partial b_r} = -m_{r,0} \cdot \left( \frac{\lambda}{\lambda_0} \right)^{-b_r} \ln \left( \frac{\lambda}{\lambda_0} \right) \frac{\partial I}{\partial m_r(\lambda)} \end{cases} \quad (12)$$

Since the last terms on the right hand of each equation can already part of UNL-VRM [66], Eq. (12) is

subsequently implemented in UNL-VRM for this study. Similar set of Eq. (12) can be applied to imaginary part of refractive index.

### 2.3. Optimized iteration and constraint

The optimized inversion model that needs to be solved can be seen as a nonlinear optimization problem as

$$\begin{aligned} \min J(\mathbf{x}) \\ \text{s.t. } \mathbf{l} \leq \mathbf{x} \leq \mathbf{u} \end{aligned} \quad (13)$$

where  $J(\mathbf{x})$  is the cost function and subject to (s.t.) some constraint conditions,  $\mathbf{l}$  and  $\mathbf{u}$  are the per-variable constants representing the lower and upper bounds for the retrieval parameter vector,  $\mathbf{x}$ , respectively. Among the classical optimization algorithms, Quasi-Newton methods are effective algorithms for finding local maximum and minimum of the objective function [80]. Compared with the traditional Newton's method, the Hessian matrix in Quasi-Newton could be updated by analyzing successive gradient vectors instead, and the general iteration formula as

$$\mathbf{x}_{k+1} = \mathbf{x}_k - \alpha_k \mathbf{B}_k^{-1} \nabla_{\mathbf{x}} J(\mathbf{x}_k) = \mathbf{x}_k - \alpha_k \mathbf{H}_k \nabla_{\mathbf{x}} J(\mathbf{x}_k) \quad (14)$$

where  $\mathbf{x}_k$  is the  $k^{\text{th}}$  step's iterated vector result,  $\nabla_{\mathbf{x}} J(\mathbf{x}_k)$  means the gradient vector of  $\nabla_{\mathbf{x}} J(\mathbf{x}_k)$  with  $\mathbf{x} = \mathbf{x}_k$ ,  $\mathbf{B}$  represents the Hessian matrix for Newton's method,  $\mathbf{H}$  means the constructed inverse matrix of  $\mathbf{B}$  with successive gradient vectors,  $\alpha$  is the iterated step length, and the subscript  $k$  means the  $k^{\text{th}}$  step's iteration. While the iteration results satisfy the condition that  $\|\mathbf{x}_{k+1} - \mathbf{x}_k\| \leq \varepsilon$ , the iteration can be seen as convergence and  $\varepsilon$  is a threshold for convergence.

Limited-memory BFGS (L-BFGS) is an optimization algorithm in the family of Quasi-Newton methods. Compared with the original Broyden–Fletcher–Goldfarb–Shanno (BFGS) algorithm, L-BFGS can use a limited amount of computer memory by storing only a few vectors that represent the approximation to the inverse Hessian matrix implicitly, which is particularly well suited for large optimization problems with a few variables. Based on L-BFGS, the L-BFGS-B algorithm extends to handle simple box constraints on variables, just as the constraints of the form  $\mathbf{l} \leq \mathbf{x} \leq \mathbf{u}$  in Eq. (13). The L-BFGS-B algorithm has been implemented in a Fortran subroutines toolbox for solving the large-scale bound constrained optimization problem [81,82]. Consequently, in our developed inversion model, the L-BFGS-B code is directly used in the inversion for optimized iteration with the inputs of cost function  $J(\mathbf{x})$  and gradient vectors  $\nabla_{\mathbf{x}} J(\mathbf{x})$ , as well as the setting of boundary constraints  $\mathbf{l}$  and  $\mathbf{u}$ . As for the practical definition of the constraint of weighting coefficients vector for surface, we will discuss in the next session.

### 2.4. Inversion theory and cost function

For the inversion theory, let  $\mathbf{x} = [x_1, \dots, x_n]^T$  denote a state vector that contains  $n$  parameters to be retrieved (such as the aerosol parameters and PCs' weighting coefficients for surface reflectance), and  $\mathbf{y} = [y_1, \dots, y_d]^T$  denote an observation vector with  $d$  elements of

measurements (such as the hyperspectral radiance). Besides, let  $\mathbf{F}$  represent a forward model (such as UNL-VRM) that describes the physics on how  $\mathbf{y}$  and  $\mathbf{x}$  are related, we have

$$\mathbf{y} = \mathbf{F}(\mathbf{x}) + \boldsymbol{\epsilon} \quad (15)$$

where  $\boldsymbol{\epsilon}$  is an experimental error that includes observation noise and forward modeling uncertainty [61]. Under the assumption of Gaussian-distributed errors and according to the maximum likelihood method, the optimized solution of Eq. (14) can be equivalent to the vector that minimizes the scalar-valued cost function:

$$J(\mathbf{x}) = \frac{1}{2}[\mathbf{y} - \mathbf{F}(\mathbf{x})]^T \mathbf{S}_{\boldsymbol{\epsilon}}^{-1} [\mathbf{y} - \mathbf{F}(\mathbf{x})] + \frac{1}{2}\gamma(\mathbf{x} - \mathbf{x}_a)^T \mathbf{S}_a^{-1} (\mathbf{x} - \mathbf{x}_a) \quad (16)$$

where  $T$  means the transpose operation,  $\mathbf{S}_{\boldsymbol{\epsilon}}$  is the covariance matrix of the error from both the measurements and the forward model,  $\mathbf{S}_a$  is the error covariance matrix of the *a priori* estimate  $\mathbf{x}_a$ , and  $\gamma$  is the regularization parameter. Thus, the gradient vector:

$$\nabla_{\mathbf{x}} J(\mathbf{x}) = -\mathbf{K}^T \mathbf{S}_{\boldsymbol{\epsilon}}^{-1} [\mathbf{y} - \mathbf{F}(\mathbf{x})] + \gamma \mathbf{S}_a^{-1} (\mathbf{x} - \mathbf{x}_a), \quad (17)$$

here,  $\mathbf{K} = \nabla_{\mathbf{x}} \mathbf{F}(\mathbf{x})$  means the Jacobian matrix of  $\mathbf{F}(\mathbf{x})$  with respect to  $\mathbf{x}$ , and its element can be written as  $K_{j,i} = \frac{\partial y_j}{\partial x_i}$ , ( $i = 1, \dots, n$ ;  $j = 1, \dots, d$ ).

In our framework, the retrieval parameters can include total aerosol volume ( $V_{\text{total}}$ ), fine volume fraction ( $\text{fmf}_V$ ), particle size distribution ( $r_{\text{eff}}^f, v_{\text{eff}}^f, r_{\text{eff}}^c, v_{\text{eff}}^c$ ) and the coefficients of refractive index ( $m_{r,0}^f, b_r^f, m_{i,0}^f, b_i^f, m_{r,0}^c, b_r^c, m_{i,0}^c, b_i^c$ ) for fine and coarse mode respectively, as well as the PCs' weighting coefficients vector  $\mathbf{w}$ . Therefore,

$$\mathbf{x} \in \{V_{\text{total}}, \text{fmf}_V, r_{\text{eff}}^f, v_{\text{eff}}^f, r_{\text{eff}}^c, v_{\text{eff}}^c, m_{r,0}^f, b_r^f, m_{i,0}^f, b_i^f, m_{r,0}^c, b_r^c, m_{i,0}^c, b_i^c, \mathbf{w}\}. \quad (18)$$

Generally, we can assume there is no correlation between the errors of retrieval parameters, and hence, the error covariance matrix  $\mathbf{S}_a$  corresponding to  $\mathbf{x}$  and  $\mathbf{x}_a$  can be seen as a diagonal matrix. For the observation error covariance matrix  $\mathbf{S}_{\boldsymbol{\epsilon}}$ , it consists of two parts:

$$\mathbf{S}_{\boldsymbol{\epsilon}} = \mathbf{S}_y + \mathbf{K}_b \mathbf{S}_b \mathbf{K}_b^T, \quad (19)$$

where  $\mathbf{S}_y$  means the uncertainty occurring in the measuring process,  $\mathbf{S}_b$  means the error covariance matrix for a vector  $\mathbf{b}$  of forward model that are not contained in  $\mathbf{x}$  but quantitatively influence the measurements of sensor,  $\mathbf{K}_b$  is the Jacobians matrix of measurements  $\mathbf{y}$  with respect to  $\mathbf{b}$ . Here,  $\mathbf{S}_y$  usually has zero off-diagonal elements with the assumption that errors are independent between measurements. Similarly, errors for  $\mathbf{b}$  are assumed to be non-correlated, thus  $\mathbf{S}_b$  will be also a diagonal matrix, so in this way,  $\mathbf{S}_y$  could be determined [67].

Since the inverse problem is to solve  $\mathbf{x}$  from the measurement  $\mathbf{y}$ , we denote the solution (*a posteriori*) as  $\hat{\mathbf{x}}$ , and the corresponding error covariance matrix can be given by

$$\hat{\mathbf{S}} = \left( \mathbf{K}^T \mathbf{S}_{\boldsymbol{\epsilon}}^{-1} \mathbf{K} + \mathbf{S}_a^{-1} \right)^{-1}, \quad (20)$$

here  $\hat{\mathbf{S}}$  describes the statistical uncertainties in retrieved  $\hat{\mathbf{x}}$  due to measurement noise and forward modeling uncertainty [61,67]. With  $\hat{\mathbf{S}}$ , we can further estimate the

uncertainty for those parameters that can be fully determined by parameter in  $\mathbf{x}$  but are not directly retrieved, such as the surface reflectance at each wavelength in this framework. Due to the surface reflectance  $r_{\lambda_i}$  only depend on the weighting coefficients vector  $\mathbf{w}$ , and does not depend those aerosols parameters in  $\mathbf{x}$ , thus

$r_{\lambda_i} = r_{\lambda_i}(\mathbf{x}) = r_{\lambda_i}(\mathbf{w})$ , ( $i = 1, \dots, d$ ). Therefore, the uncertainty of  $r_{\lambda_i}$  can be written as

$$\epsilon_{r_{\lambda_i}} = \sqrt{\sum_{j=1}^n \sum_{k=1}^n \hat{\mathbf{S}}_{j,k} \frac{\partial r_{\lambda_i}}{\partial x_j} \frac{\partial r_{\lambda_i}}{\partial x_k}} = \sqrt{\sum_{j=1}^m \sum_{k=1}^m \hat{\mathbf{S}}_{j,k} \frac{\partial r_{\lambda_i}}{\partial w_j} \frac{\partial r_{\lambda_i}}{\partial w_k}}, \quad (i = 1, \dots, d), \quad (21)$$

combined Eq. (6) and Eq. (21), we have

$$\epsilon_{r_{\lambda_i}} = \sqrt{\sum_{j=1}^m \sum_{k=1}^m \hat{\mathbf{S}}_{j,k} P_{ij} P_{ik}}, \quad (i = 1, \dots, d), \quad (22)$$

here  $P$  is an element of the PC matrix, and the definition is same as in Section 2.1.

### 3. Data and experiment design for green vegetation and rangeland

To test our algorithm presented in Section 2, we designed a series of experiments, focusing on green vegetation and rangeland surfaces for which intensive observation data for their spectral characteristics is available. As described below (Section 3.1), data on aerosol

properties used in the forward calculation is from literature such as Xu and Wang [67]. The characterization of prior error is discussed in Section 3.2.

#### 3.1. Surface and aerosol data

PCA is conducted for the spectral dataset of green vegetation and rangeland surfaces that are part of USGS digital spectral library [65]. Fig. 3(a) and (b) presents the spectral curves from  $n_s = 54$  kinds (samples) of vegetation and  $n_s = 87$  kinds of rangeland dataset, respectively. In the analysis, we have interpolated the original spectral datasets into the wavelength of GEO-TASO in visible band, and hence, the dimension or the number of wavelengths for each spectral curve  $d$  is set as 1000. Table 3 also gives the BRDF parameters at 470, 550 and 650 nm wavelengths for a typical vegetation surface region from the BRDF product of MODIS.

**Table 3**  
BRDF parameters for a vegetation-type surface.

Wavelength (nm)	$f_{iso}(\lambda)$	$k_1(\lambda)$	$k_2(\lambda)$
470	0.041	0.011	0.010
550	0.081	0.022	0.035
650	0.064	0.018	0.012

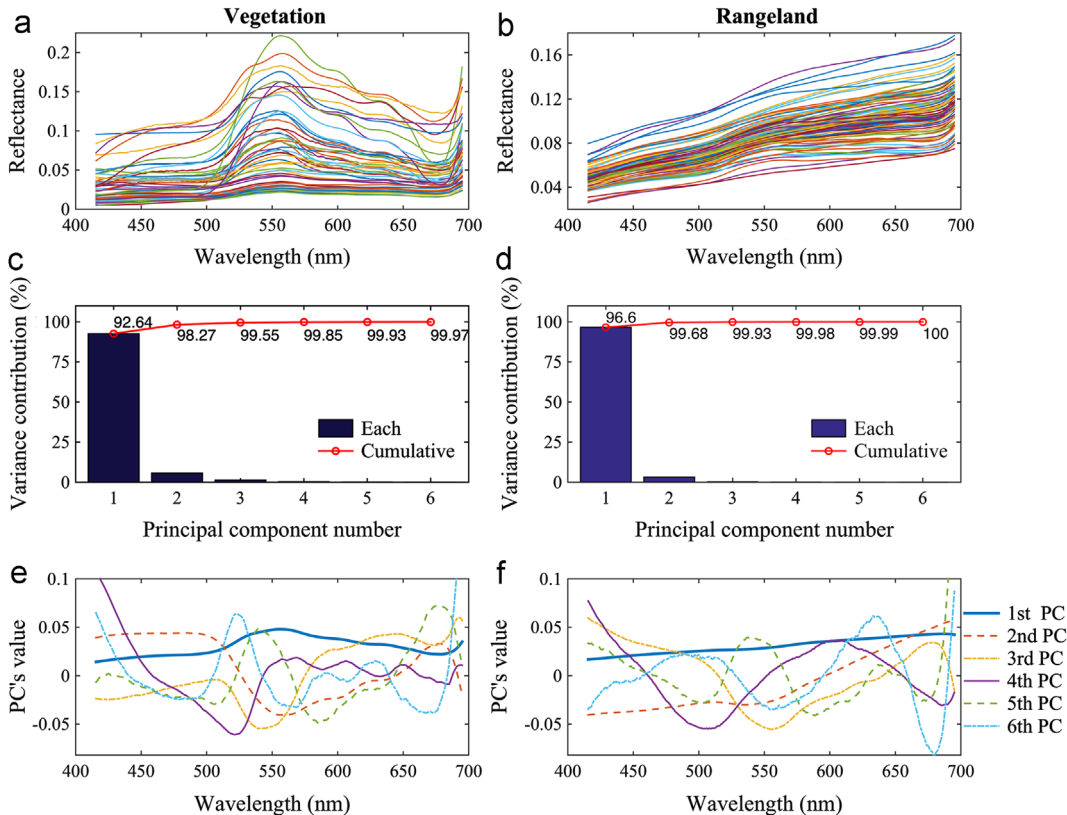


**Fig. 3.** Principal component analysis results respectively for vegetation dataset (left panel) and rangeland dataset (right panel). (a–b) Spectra of surface reflectance acquired from the USGS spectral library. (c–d) Contribution of the first 6 principal components to the total variance. (e–f) Spectra of the first 6 principal components.

Our forward calculation follows Xu and Wang [67] for a typical mid-latitude summer atmospheric profile. The aerosol properties used in the forward simulation are listed in Table 4, including particle size parameters, effective radius  $r_{\text{eff}}$ , effective variance  $v_{\text{eff}}$ , and refractive indices ( $m_r, m_i$ ) for fine and coarse mode. The fine-mode particles are corresponding to water-soluble aerosols from Optical Properties of Aerosols and Clouds (OPAC) database [83], while the coarse-mode is assumed for large spherical particles with refractive index from the work of Patterson et al. [84] and Wanger et al. [85]. Meanwhile, we also set the total volume concentration  $V_{\text{total}} = 0.149 \mu\text{m}^3 \mu\text{m}^{-2}$  and the volume fine mode fraction  $\text{fmf}_V = 0.8$ ; the aerosol is a fine-dominated model and aerosol volume can be scaled as necessary to maintain a normalized AOD  $\tau_a = 1$  at 440 nm corresponding to a moderate hazy condition. In addition, the refractive index corresponding to the each wavelength could be gained by the nonlinear interpolation

**Table 4**  
Aerosol parameters used in the forward simulations.

Parameters	Fine mode	Coarse mode
$r_{\text{eff}}$ ( $\mu\text{m}$ )	0.21	1.90
$v_{\text{eff}}$ ( $\mu\text{m}$ )	0.25	0.41
$m_r$	1.44, 1.44	1.56, 1.55
$m_i$	0.009, 0.011	0.004, 0.003

The refractive index  $m_r$  and  $m_i$  are at 440 nm and 675 nm wavelengths, respectively.

given in Eq. (11) with the results shown in Table 4; the four parameters in Eq. (11) are approximately calculated from the Aerosol Robotic Network (AERONET) results at 440 nm and 675 nm. As for the surface reflectance, because GEOTASO is a single angle measurement, the Lambertian surface curve is considered from the dataset shown in Fig. 3.

### 3.2. Characterization of the a priori error

As the first part of this series of studies, here we focus on the development and self-consistent check of the theoretical framework we developed. Hence, the ability of inversion algorithm to retrieve the weighting coefficients vector for the construction of hyperspectral surface reflectance is evaluated, in which all the aerosol properties are assumed to be well characterized within certain uncertainty. Use of this framework to analyze the information content of aerosol parameters (such as total volume concentration, particle size distribution, and refractive index) contained in the hyperspectral measurements will be presented in the next paper. We set the state vector only containing a few weighting coefficients elements corresponding to the surface reflectance as  $\mathbf{x} = [w_1, \dots, w_n]^T$ ; and for a priori estimate  $\mathbf{x}_a$ , we consider the averaged results of the entire weighting coefficients vector for the corresponding surface type. Meanwhile, based on the discussion in subsection 2.4, the error covariance matrix  $\mathbf{S}_a$  is set as a diagonal matrix as  $\text{diag}(\sigma_{w_1}^2, \dots, \sigma_{w_n}^2)$ , here  $\sigma_{w_i}$  is the standard variance of weighting coefficient  $w_i$ , ( $i = 1, \dots, n$ ) for the given surface type.

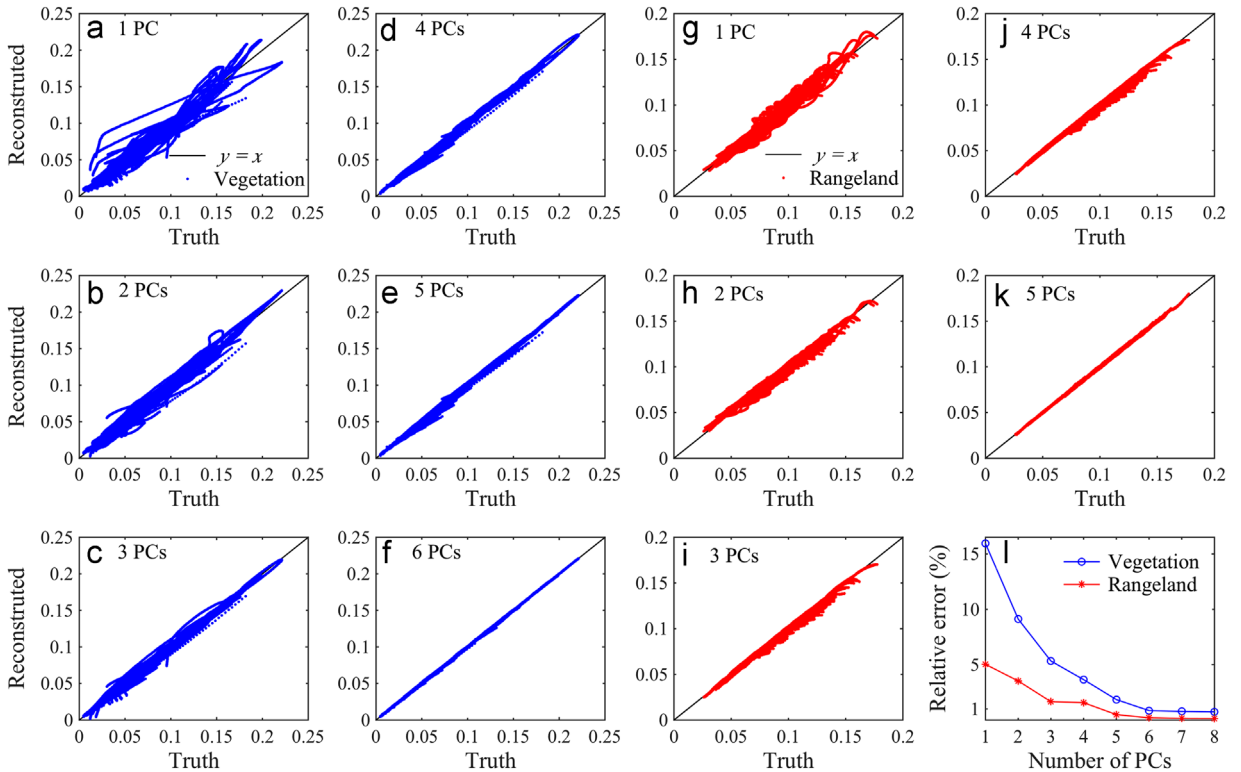


**Fig. 4.** (a–f) Scatterplots of the reconstructed reflectance with the 1st to 6th PCs versus actual reflectance of the vegetation surface dataset over 1000 spectral wavelengths from 415 nm to 696 nm. (g–k) Same as (a)–(f) but for the rangeland surface dataset reconstructed with the 1st to 5th PCs; (l) the average relative error in reconstructed reflectance of vegetation and rangeland surface as a function of number of PCs.

For the observation error covariance matrix  $\mathbf{S}_e$ , we have assumed that the aerosol particles are well characterized, consequently the contribution of term  $\mathbf{K}_b \mathbf{S}_b \mathbf{K}_b^T$  to  $\mathbf{S}_e$  in Eq. (19) could be ignored; this assumption is set only for the self-consistent check of the implementation of theoretical development in this study. Consequently, considering the measurement's error at each wavelength, we have

$$(\mathbf{S}_e)_{jj} \approx (\mathbf{S}_y)_{jj} = S_{y_j} = (e_j \times I_j^{\text{mea}})^2, \quad (j = 1, \dots, d), \quad (22)$$

here  $e_j$  means the relative errors of measurements at each wavelength and is set as  $e_j = 2\%$  in this study; the subscript  $j$  represents the number of wavelength. The actual formula of cost function could be constructed as

$$J(\mathbf{x}) = \frac{1}{2} \sum_{j=1}^d (I_j^{\text{mea}} - I_j^{\text{mod}})^2 / S_{y_j} + \frac{1}{2} \sum_{i=1}^n (w_i - \bar{w}_i)^2 / S_{w_i}, \quad (23)$$

$$\nabla_{\mathbf{x}} J(\mathbf{x}) = \begin{bmatrix} -\sum_{j=1}^d \frac{\partial I_j^{\text{mod}}}{\partial w_1} (I_j^{\text{mea}} - I_j^{\text{mod}}) / S_{y_j} + (w_1 - \bar{w}_1) / S_{w_1} \\ \vdots \\ -\sum_{j=1}^d \frac{\partial I_j^{\text{mod}}}{\partial w_n} (I_j^{\text{mea}} - I_j^{\text{mod}}) / S_{y_j} + (w_n - \bar{w}_n) / S_{w_n} \end{bmatrix}, \quad (24)$$

where  $I$  denotes the normalized TOA radiance, superscript "mea" and "mod" represent the results measured at-sensor and calculated by for forward model respectively, and the regularization parameter  $\gamma = 1$ .

## 4. Results

### 4.1. PCA results and validation

Fig. 3(c) and (d), respectively, illustrates the contribution rate of each PC for two different spectral samples corresponding to vegetation and rangeland, respectively. For vegetation dataset, the total contribution rate could reach 99.97% with 6 PCs; likewise, 6 PCs' contribution could make nearly 100% contribution for rangeland spectra. Fig. 3(e) and (f) further plot each corresponding value of these first 6 PCs.

In order to demonstrate that 6 PCs can present the variation of spectral reflectance with good accuracy, the cross validation is conducted in which  $n-1$  spectral sample curves are selected for PCA to obtain the PCs, and the remaining spectra curve (not used in PCA) is used to get the corresponding weighting coefficients vector  $\mathbf{w}$ . With this approach, the reconstructed results of the remaining spectra could be gained and compared with the actual spectra. By this leave-out-one cross validation, we can evaluate the accuracy of reconstructed spectra  $n$  times. Fig. 4(a)–(f) shows the scatterplots between the truth vegetation surface reflectance and the reconstructed results at 1000 wavelengths from using 1 PC up to using 6 PCs respectively. Similarly, Fig. 4(g)–(k) presents the comparison scatterplots between the truth and reconstructed spectra for rangeland surfaces from using 1 PC up to 5 PCs, respectively. Furthermore, subsets in Fig. 4

(l) illustrate the average relative error of vegetation and rangeland as a function of number of PCs, in which the

averaged relative error is define as  $\frac{\sum_{i=1}^{n_s} \sum_{j=1}^d \frac{|r_{ij} - \hat{r}_{ij}|}{r_{ij}}}{n_s \times d}$ , here  $r_{ij}$  means the reflectance in the  $j^{\text{th}}$  band (dimension) of the  $i^{\text{th}}$  spectral curve (sample), the superscript "r" represents the reconstructed results, and  $n_s$  is the number of samples. From this figure, we can see that the averaged relative error decrease as the number of PCs increase; for 1% error accuracy, 6 and 5 PCs should be used for vegetation and rangeland respectively.

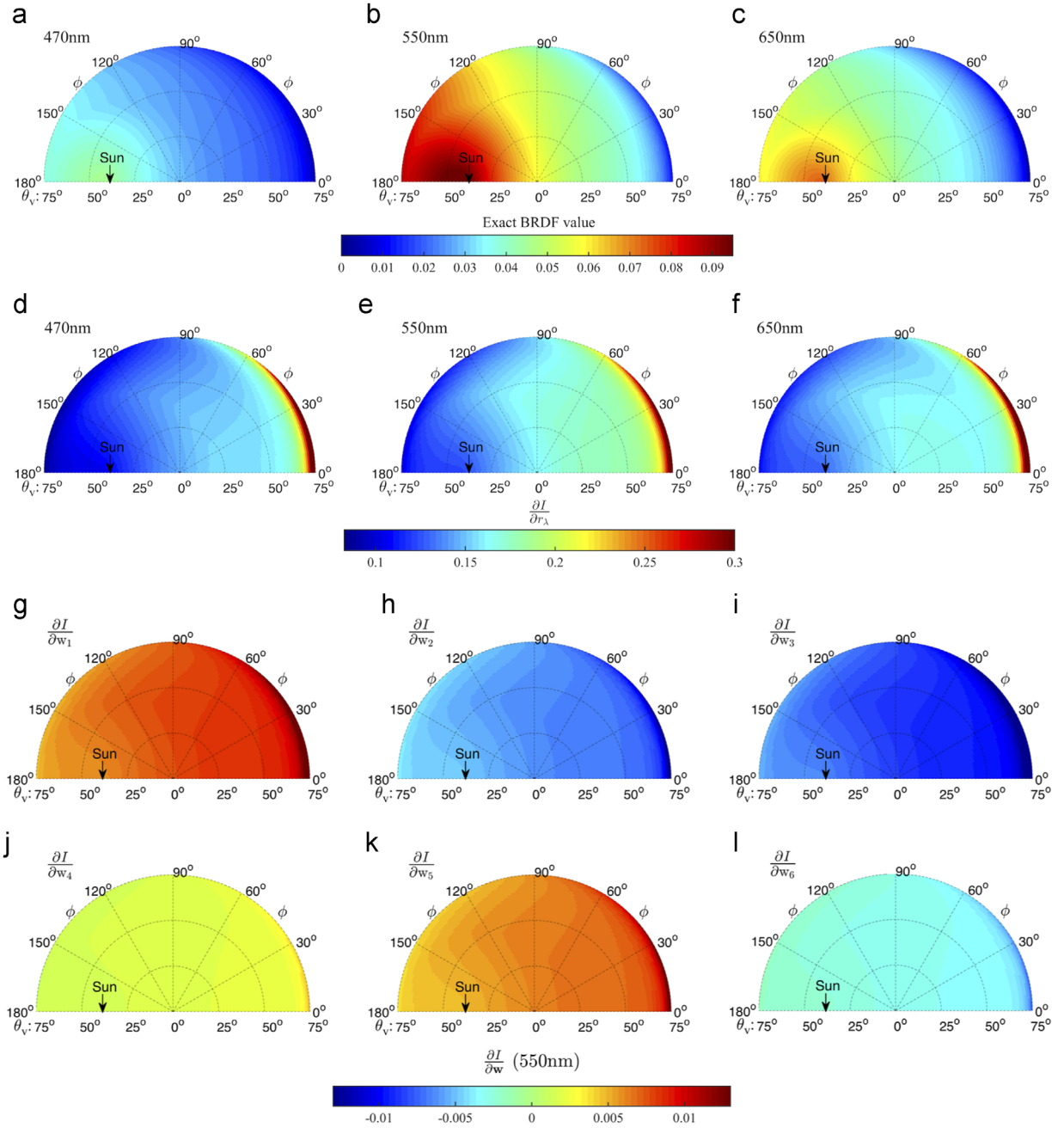
### 4.2. Variation of Jacobians with BRDF considered

Fig. 5(a)–(c) shows the polar-plot of simulated results of BRDF surface reflectance. In the polar-plot, the radius represents the viewing zenith angle ( $\theta_v$ ) and the polar angle denotes the relative azimuth angle ( $\phi$ ). The solar zenith angle  $\theta_0 = 40^\circ$  is used in the calculation for Fig. 5.  $\phi = 180^\circ$  means the observer and Sun are in the same direction and in the same side of the main plane. Obviously, the backscattering is brighter that forward scattering for the vegetation surface, especially around those angles regions where  $\theta_v = \theta_0$ . Corresponding to the BRDF results, Fig. 5(d)–(f) illustrates the Jacobians results of  $\frac{\partial I}{\partial r_i}$  calculated by Eq. (9) and UNL-VRM simulations. Following the results of  $\frac{\partial I}{\partial r_i}$  at 550 nm as an example, Fig. 5(g)–(l) gives the Jacobians polar-plot of  $\frac{\partial I}{\partial \mathbf{w}}$  calculated by Eq. (7) for BRDF case. We can find that the smaller the BRDF surface reflectance is, the larger the value of  $\frac{\partial I}{\partial r_i}$  would be. For example, in those angle regions with brighter reflectance, most of Jacobians are smaller than 0.12, while for those angle regions with darker reflectance, most of Jacobians are larger than 0.18 and even larger. Similarly, the larger the BRDF is, the larger the absolute value of  $\frac{\partial I}{\partial \mathbf{w}}$  would be.

### 4.3. Validation of Jacobians

We validate the Jacobians produced by UNL-VRM with a simple finite-difference test (usually with 0.1% disturbance) to UNL-VRM. Fig. 6(a)–(f) shows the scatterplot case of Jacobian results at 1000 visible wavelengths by the finite difference derived and analytic means from the first weighting coefficient  $w_1$  to the sixth coefficient  $w_6$  respectively with the averaged reflectance spectra of vegetation. Similarly, Fig. 6(h)–(l) gives another scatterplot case with the averaged reflectance spectra of rangeland. From those results, the finite-difference derived Jacobian and analytic Jacobian results are in good agreement for each coefficient, and the averaged relative error of six coefficients at each wavelength is smaller than 0.1%.

Fig. 7(a)–(c) shows the comparison of Jacobians  $\frac{\partial I}{\partial r_i}$  with BRDF included in UNL-VRM using the analytical method with those computed from UNL-VRM using finite difference estimates with 0.1% disturbance of  $r_i$  for different viewing angles (Fig. 5(a)–(c)) at 3 given bands (470, 550, 650 nm), while Fig. 7(e)–(f) is for 3 given



**Fig. 5.** (a–c) UNL-VRM simulated BRDF reflectance of a green vegetated surface at 470, 550, and 650 nm, respectively. (d–f) UNL-VRM calculated Jacobians of TOA radiance with respect to surface reflectance ( $\frac{\partial I}{\partial r_\lambda}$ ) corresponding to panels (a)–(c). (g–i) UNL-VRM calculated Jacobians of TOA radiance with respect to PC’s weighting coefficient ( $\frac{\partial I}{\partial w}$ ) from  $w_1$  to  $w_6$  based on the results shown in panel (e).

viewing angles at 1000 visible bands (415–696 nm). The relative errors are all smaller than 0.2% in Fig. 7.

Also with 0.1% disturbance of the coefficients, Fig. 8 illustrates the comparison of Jacobians for the coefficient of refractive index (e.g., 4 parameters in Eq. (12)) at 1000 visible bands calculated with UNL-VRM using the analytical method with those computed from UNL-VRM using finite difference estimates for the fine and coarse mode respectively. It shows that the two results agree well with an error smaller than 0.2%.

#### 4.4. Retrieval demonstration and self-consistent check

Synthetic TOA reflectances ( $\rho^{TOA}$ ) are first computed for two spectral reflectance curves for vegetation ( $\rho_{v1}^s, \rho_{v2}^s$ ) and two spectral curves for rangeland surface dataset ( $\rho_{r1}^s, \rho_{r2}^s$ ), respectively. Forward simulations by UNL-VRM following the wavelengths of GEO-TASO from 415 nm to 695 nm at the 0.18 nm resolution are conducted, and the weighting coefficients ( $w_1$ – $w_6$ ) of PCs for test vegetation and rangeland surface types are given in Table 6. After that, we add

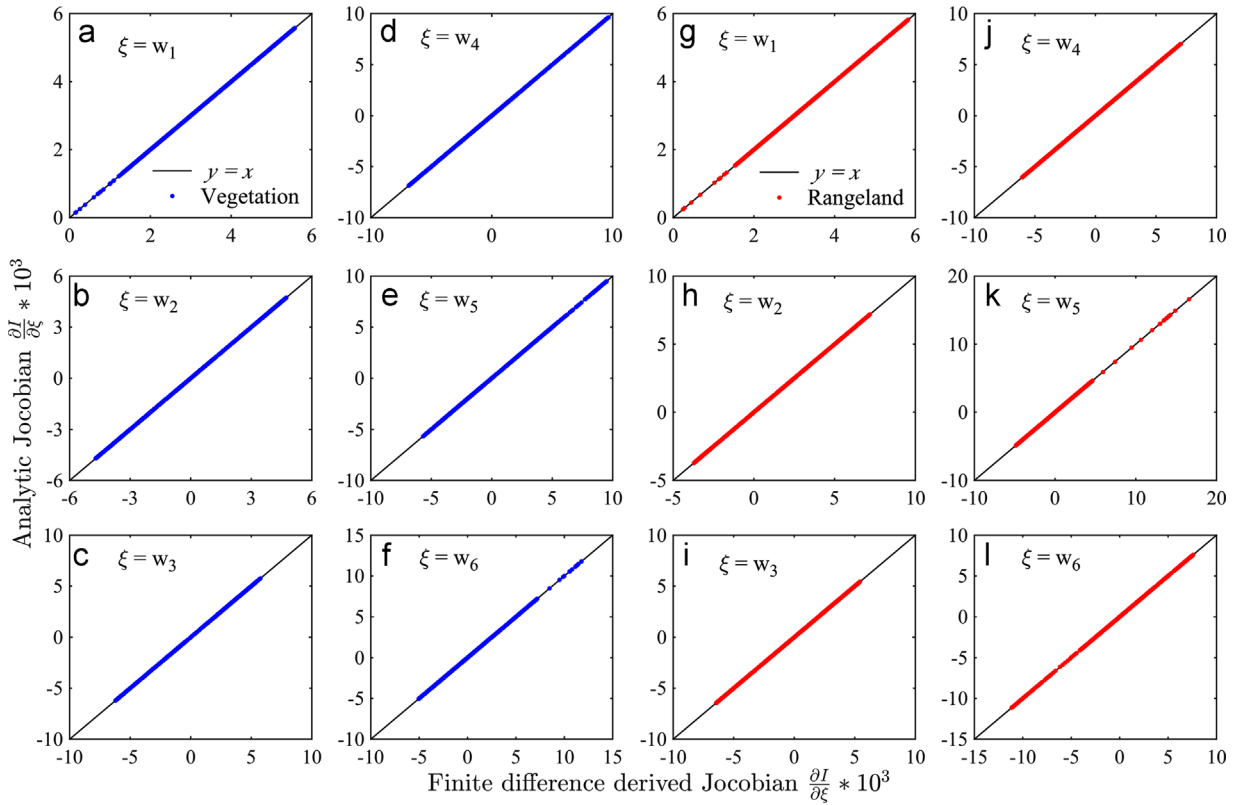


**Fig. 6.** Validation of UNL-VRM analytical Jacobians of radiance with respect to the PC's weighting coefficient ( $w_1$ – $w_6$ ) against the Jacobians derived by finite difference. Each scatter indicates the Jacobian at one of the 1000 spectral wavelengths from 415 nm to 696 nm with the same observation geometries ( $\theta_0 = 40^\circ$ ,  $\theta_v = 30^\circ$ ,  $\phi = 20^\circ$ ). Panels (a)–(f) are for a vegetation surface, and (g)–(l) for a rangeland surface.

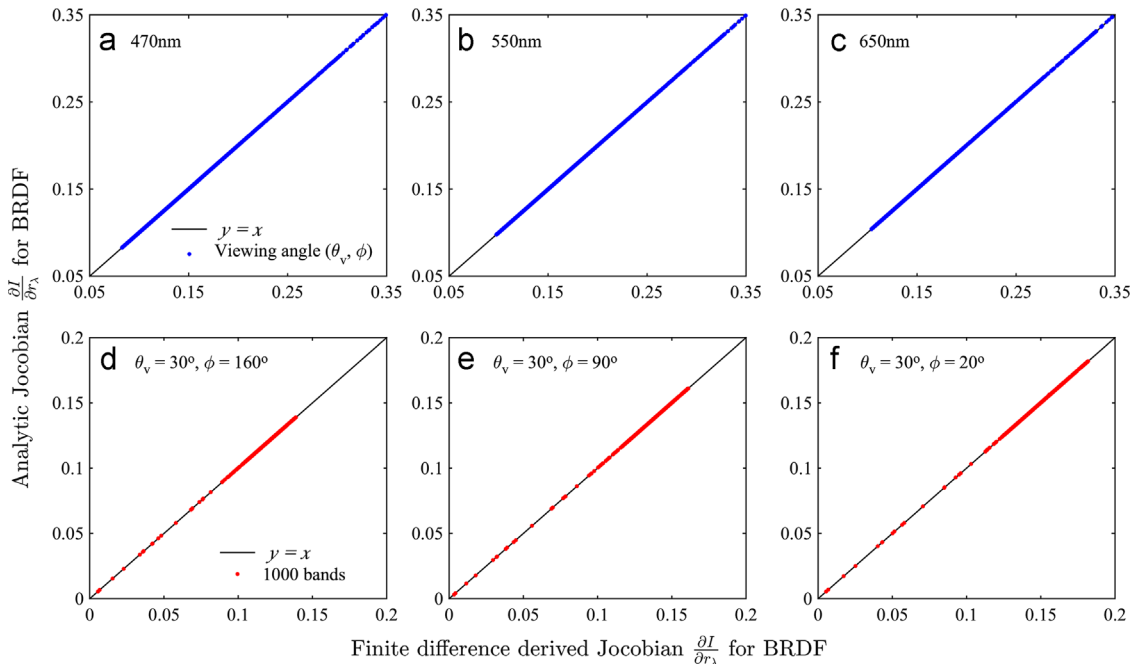


**Fig. 7.** Same as the Fig. 6 but for the validation of Jacobians ( $\frac{dI}{d\theta_v}$ ) for BRDF at  $\theta_0 = 40^\circ$ . Panels (a)–(c) are for the wavelengths of 470, 550, 650 nm respectively, each scatter indicates the Jacobian at one of the viewing angle ( $\theta_v$ ,  $\phi$ ), in which the viewing zenith  $\theta_v = 0^\circ$ – $75^\circ$  and  $\phi = 0^\circ$ – $180^\circ$  with an increment of  $1^\circ$ . Panels (d)–(f) are for the cases of given viewing angles as shown in the figure, each scatter indicates the Jacobian at one of the 1000 spectral bands.

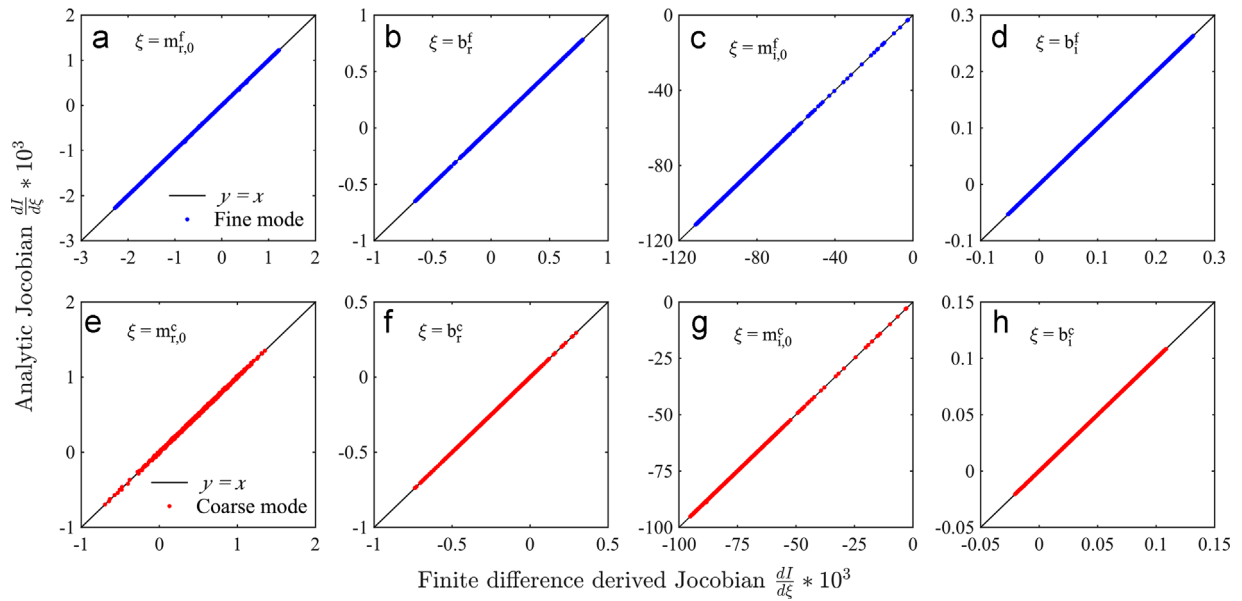


Fig. 8. Same as the Fig. 6 but for the validation of Jacobians to the coefficients of aerosol refractive index ( $m_{r,0}$ ,  $b_r$ ,  $m_{i,0}$  and  $b_i$ ) respectively. Panels (a)–(d) are for the fine mode, while panels (e)–(h) are for the coarse mode.

Table 5

The mean ( $\bar{w}$ ), standard variation ( $\sigma_w$ ), lower ( $l$ ) and upper ( $u$ ) bounds of each PC's weighting coefficients for vegetation and rangeland surfaces.

Weighting coefficient	Vegetation				Rangeland			
	$\bar{w}$	$\sigma_w$	$l$	$u$	$\bar{w}$	$\sigma_w$	$l$	$u$
$w_1$	1.7047	1.0766	0.5130	4.4630	2.7278	0.4937	1.6780	4.1720
$w_2$	0.0465	0.2652	-1.1330	0.6150	-0.1065	0.0798	-0.3070	0.0610
$w_3$	0.0377	0.1269	-0.2330	0.3970	-0.0875	0.0301	-0.1940	-0.0180
$w_4$	0.0362	0.0611	-0.1660	0.1920	0.0058	0.0115	-0.0340	0.0250
$w_5$	0.0398	0.0320	-0.0620	0.1290	0.0476	0.0071	0.0300	0.0700
$w_6$	0.0113	0.0198	-0.0570	0.0590	-0.0145	0.0042	-0.0270	-0.0030

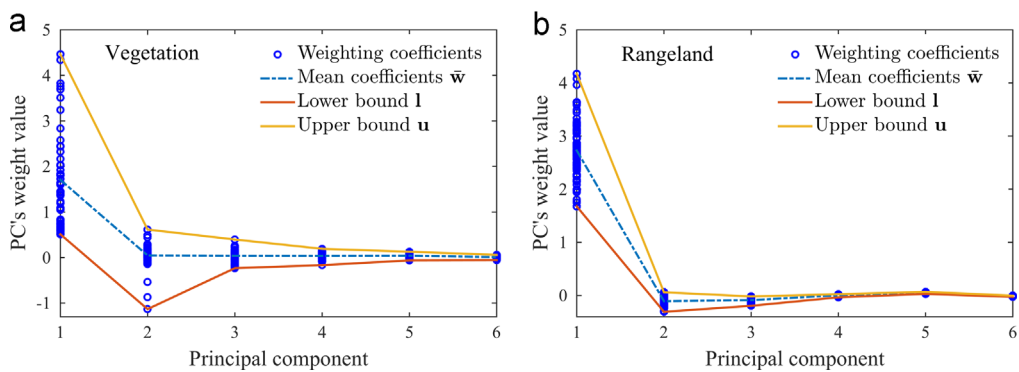


Fig. 9. Lower and upper bounds as well as mean results of the PC's coefficients for the reflectance of vegetation-type surfaces (a) and rangeland-type surfaces (b).

the 1% Gaussian noise to the simulated TOA radiance and further convert it to the assumed TOA reflectance, respectively denoted as  $\rho_{v1}^{TOA}$ ,  $\rho_{v2}^{TOA}$ ,  $\rho_{r1}^{TOA}$  and  $\rho_{r2}^{TOA}$ . Fig. 9 and Table 5 further show the mean and standard variance

( $\bar{w}$ ,  $\sigma_w$ ) of weighting coefficients, as well as their corresponding lower ( $l$ ) and upper ( $u$ ) bounds.

A comparison is summarized in Fig. 10 between the retrieved surface reflectance curves reconstructed from

using retrieved 6 weighting coefficients and the true spectral curve used in for the synthetic data, indicating a good agreement with correlation coefficient ( $R$ ) of larger than 0.99 and the root mean square error ( $rmse$ ) of less than 0.003 for all four cases. In addition, the retrieval uncertainties of the surface reflectance at each wavelength calculated by Eq. (22) for those four cases are all smaller than 2% (with the assumption of 2% measurement errors). Fig. 11 shows the simulated TOA reflectance and the normalized cost function during each of five steps for iteration and convergence before the cost function in the iteration is

**Table 6**

The weighting coefficients of test surface reflectance spectra of vegetation and rangeland.

Weighting coefficient	Vegetation		Rangeland	
	v1	v2	r1	r2
$w_1$	1.6518	3.5926	3.4065	2.0984
$w_2$	0.0637	-0.0069	-0.1079	-0.1471
$w_3$	-0.0052	0.0819	-0.0863	-0.0907
$w_4$	0.0489	0.0290	0.0030	0.0044
$w_5$	0.0426	0.0350	0.0468	0.0460
$w_6$	0.0180	0.0028	-0.0157	-0.0152

minimized. A more than 99% reduction of the cost function is achieved after the convergence.

## 5. Summary and conclusion

As the first part of a series of studies for retrieving aerosol properties from the hyperspectral radiances measured by a newly developed hyperspectral instrument GEO-TASO in the visible bands, we develop a theoretical framework of the inversion algorithm for hyperspectral remote sensing of aerosol particles based on PCA combined with UNL-VRM model. This framework builds upon UNL-VRM but with the new developments for (a) PCA, (b) computing the Jacobians of TOA reflectance with respect to the weighting coefficients of surface reflectance principal components, and (c) computing the Jacobians of TOA reflectance to the parameters related the wavelength dependence of aerosol refractive index. For (b), the computation can also include BRDF, assuming that the PC remains the same regardless of the geometry. For (c), we assume the variation of refractive index with wavelength following a power-law approximation, and hence, only four parameters (e.g., real and imaginary part of refractive

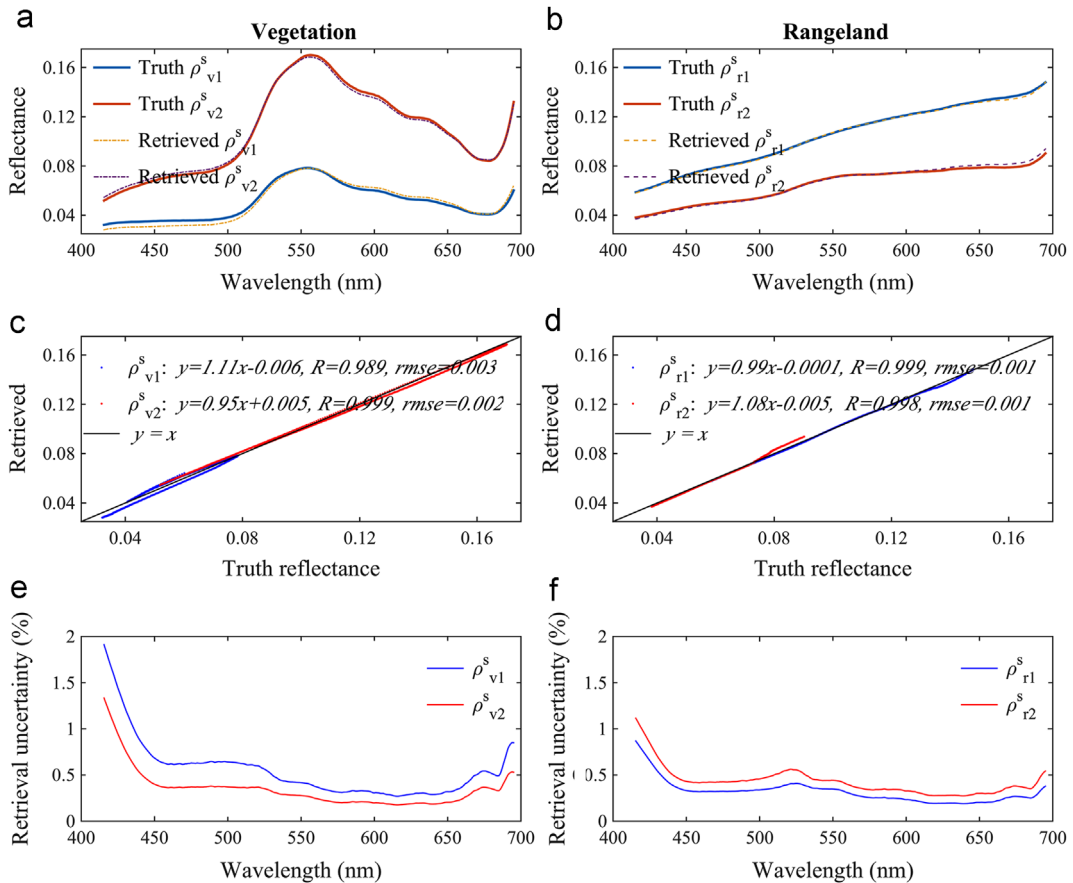


**Fig. 10.** Comparison of the retrieved surface reflectance using 6 PCs with the prescribed truth for vegetation cases (left panels) and rangeland cases (right panels), respectively. Upper panels (a),(b) show the surface reflectance as a function of wavelength, and the middle panels (c),(d) present scatterplots, in which each scatter indicated the surface reflectance at one of 1000 spectral wavelengths. Lower panels (e),(f) show the retrieval uncertainty of surface reflectance.

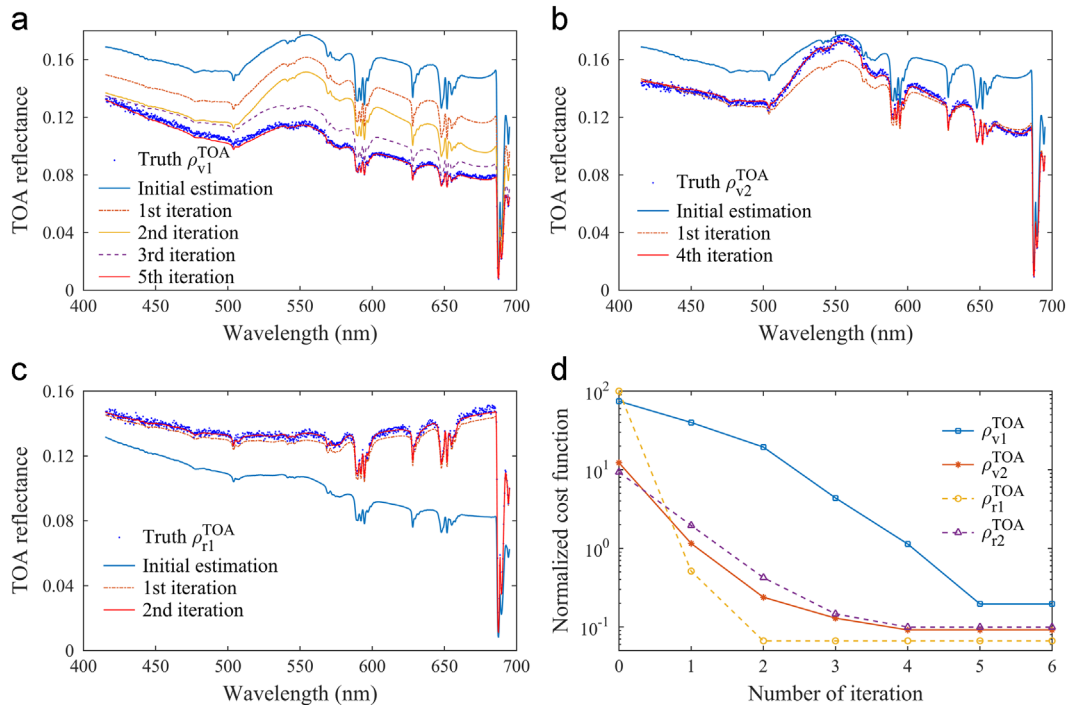


**Fig. 11.** The iterative process of TOA reflectance and the convergence of cost function in the optimized inversion, (a) and (b) are for two vegetation cases (i.e.,  $\rho_{v1}^{TOA}$  and  $\rho_{v2}^{TOA}$ ), respectively, (c) is for one rangeland case ( $\rho_{r1}^{TOA}$ ), the other rangeland case ( $\rho_{r2}^{TOA}$ ) is not shown here, (d) plots the reduction of normalized cost functions along the number of iterations.

index at base wavelength as well as their corresponding power-law coefficients) are needed in the retrieval.

By considering the green vegetation and rangeland surface spectral dataset from the USGS digital spectral library, the spectral reconstructions by PCA show that the reconstruction of surface reflectance using the first six weighting coefficients of principal components can yield the relative errors all smaller than 1%. The analytical calculation of Jacobians in UNL-VRM is then compared with the counterparts from finite-difference calculations, and they are found to be in good agreement with an uncertainty of less than 0.2%.

Finally, with an assumption that the aerosol properties are all well characterized with an overall measurement uncertainty of 2%, we conducted a self-consistent check of the retrieval framework developed in this study. The results show that the retrieved and assumed “true” spectra agree well with each other, with a correlation coefficient for most cases larger than 0.99 and the root mean square error is smaller than 0.003, as well as the retrieval uncertainties are all smaller than 2%.

The framework of this study will be used to conduct information content analysis similar as the work of Xu and Wang [67] on what aerosol parameters could be retrieved from hyperspectral measurements in the visible bands. From the information content analysis, an operational algorithm for aerosol retrievals will then be designed and tested with real data measured by GEO-TASO and TEMPO (after its launch). It should be noted that as a geostationary satellite, TEMPO offers hourly observation for each pixel, enabling more frequent sampling of the backscatter

spectra at the top of the atmosphere in conditions with low AOD, and thus better characterizing the surface spectra for each pixel. Indeed, past studies have used the minimum (or second minimum) reflectance at each pixel taken by geostationary imager within a certain time period ( $\sim 20$ – $25$  days) as the surface reflectance in the aerosol retrieval algorithm for Geostationary Operational Environmental Satellite (GOES) [86–90]. With TEMPO’s observation, a PC analysis of the backscattered spectra in low-AOD conditions can be conducted to obtain the PCs for surface reflectance at each pixel, which will facilitate the use of the hyperspectral algorithm developed here to simultaneously retrieve the aerosol properties and the weight coefficients for each surface reflectance PCs (and hence surface reflectance) from TEMPO.

## Acknowledgment

Funding for this study was provided by the NASA Earth Science Division as part of NASA’s GEO-CAPE mission study (NNX14AH10G) and Office of Naval Research (ONR’s) Multidisciplinary University Research Initiatives (MURI) Program (G-00976-3). J. Wang is grateful to Jassim (Jay) A. Al-Saadi and GEO-TASO team for their encouragement, and thanks the GEO-CAPE aerosol working group and science working group for their constructive suggestions and fruitful discussions. The Holland Computing Center of University of Nebraska – Lincoln and NASA High End Computing program are acknowledged for their help in computing.

## References

- [1] King MD, Kaufman YJ, Tanré D, Nakajima T. Remote sensing of tropospheric aerosols from space: past, present, and future. *B Am Meteorol Soc* 1999;80:2229–59.
- [2] Kokhanovsky AA, Breon FM, Cacciari A, Carboni E, Diner D, Di Nicolantonio W, et al. Aerosol remote sensing over land: A comparison of satellite retrievals using different algorithms and instruments. *Atmos Res* 2007;85:372–94.
- [3] Hauser A, Oesch D, Foppa N, Wunderle S. NOAA AVHRR derived aerosol optical depth over land. *J Geophys Res Atmos* 2005;110.
- [4] Riffer M, Popp C, Hauser A, Fontana F, Wunderle S. Validation of a modified AVHRR aerosol optical depth retrieval algorithm over Central Europe. *Atmos Meas Tech* 2010;3:1255–70.
- [5] Vidot J, Santer R, Aznay O. Evaluation of the MERIS aerosol product over land with AERONET. *Atmos Chem Phys* 2008;8:7603–17.
- [6] Hsu NC, Si-Chee T, King MD, Herman JR. Aerosol properties over bright-reflecting source regions. *IEEE Trans Geosci Remote* 2004;42:557–69.
- [7] Hsu NC, Si-Chee T, King MD, Herman JR. Deep blue retrievals of asian aerosol properties during ACE-Asia. *IEEE Trans Geosci Remote* 2006;44:3180–95.
- [8] Levy RC, Remer LA, Kleidman RG, Mattoo S, Ichoku C, Kahn R, et al. Global evaluation of the collection 5 MODIS dark-target aerosol products over land. *Atmos Chem Phys* 2010;10:10399–420.
- [9] Levy RC, Remer LA, Mattoo S, Vermote EF, Kaufman YJ. Second-generation operational algorithm: retrieval of aerosol properties over land from inversion of moderate resolution imaging spectroradiometer spectral reflectance. *J Geophys Res Atmos* 2007;112.
- [10] North PRJ. Estimation of aerosol opacity and land surface bidirectional reflectance from ATSR-2 dual-angle imagery: operational method and validation. *J Geophys Res* 2002;107.
- [11] Thomas GE, Dean SM, Carboni E, Grainger RG, Poulsen CA, Siddans R, et al. Aerosol extraction algorithm definition ATSR-2/AATSR algorithm theoretical basis document. Oxford: University of Oxford; 2005.
- [12] Kahn RA, Gaitley BJ, Garay MJ, Diner DJ, Eck TF, Smirnov A, et al. Multiangle Imaging Spectroradiometer global aerosol product assessment by comparison with the Aerosol Robotic Network. *J Geophys Res Atmos* 2010;115:33897–929.
- [13] Kahn RA, Gaitley BJ, Martonchik JV, Diner DJ, Crean KA, Holben B. Multiangle Imaging Spectroradiometer (MISR) global aerosol optical depth validation based on 2 years of coincident Aerosol Robotic Network (AERONET) observations. *J Geophys Res Atmos* 2005;110.
- [14] Herman M, Deuzé JL, Devaux C, Goloub P, Bréon FM, Tanré D. Remote sensing of aerosols over land surfaces including polarization measurements and application to POLDER measurements. *J Geophys Res* 1997;102:17039.
- [15] Deuzé JL, Bréon FM, Devaux C, Goloub P, Herman M, Lafrance B, et al. Remote sensing of aerosols over land surfaces from POLDER-ADEOS-1 polarized measurements. *J Geophys Res Atmos* 2001;106:4913–26.
- [16] Waquet F, Cornet C, Deuzé JL, Dubovik O, Ducos F, Goloub P, et al. Retrieval of aerosol microphysical and optical properties above liquid clouds from POLDER/PARASOL polarization measurements. *Atmos Meas Tech* 2013;6:991–1016.
- [17] Griffin MK, Hsu SM, Burke H-hK, Orloff SM, Upham CA. Examples of EO-1 Hyperion Data Analysis. *Linc Lab J* 2005;15:271–98.
- [18] Holzer-Popp T. Retrieving aerosol optical depth and type in the boundary layer over land and ocean from simultaneous GOME spectrometer and ATSR-2 radiometer measurements, 1, method description. *J Geophys Res* 2002;107.
- [19] Holzer-Popp T. Retrieving aerosol optical depth and type in the boundary layer over land and ocean from simultaneous GOME spectrometer and ATSR-2 radiometer measurements 2. Case study application and validation. *J Geophys Res* 2002;107.
- [20] Hasekamp OP, Landgraf J. Linearization of vector radiative transfer with respect to aerosol properties and its use in satellite remote sensing. *J Geophys Res* 2005;110.
- [21] Hasekamp OP, Landgraf J. Retrieval of aerosol properties over the ocean from multispectral single-viewing-angle measurements of intensity and polarization: Retrieval approach, information content, and sensitivity study. *J Geophys Res* 2005;110.
- [22] Lee C, Martin RV, van Donkelaar A, O'Byrne G, Krotkov N, Richter A, et al. Retrieval of vertical columns of sulfur dioxide from SCIAMACHY and OMI: Air mass factor algorithm development, validation, and error analysis. *J Geophys Res* 2009;114.
- [23] Taha G, Rault DF, Loughman RP, Bourassa AE, von Savigny C. SCIAMACHY stratospheric aerosol extinction profile retrieval using the OMPS/LP algorithm. *Atmos Meas Tech* 2011;4:547–56.
- [24] Torres O, Tanskanen A, Veihelmann B, Ahn C, Braak R, Bhartia PK, et al. Aerosols and surface UV products from Ozone Monitoring Instrument observations: An overview. *J Geophys Res* 2007;112.
- [25] Jeong U, Kim J, Ahn C, Torres O, Liu X, Bhartia PK, et al. An online aerosol retrieval algorithm using OMI near-UV observations based on the optimal estimation method. *Atmospheric Chemistry and Physics Discussions* 2015;15:16615–54.
- [26] Peyridieu S, Chédin A, Tanré D, Capelle V, Pierangelo C, Lamquin N, et al. Saharan dust infrared optical depth and altitude retrieved from AIRS: a focus over North Atlantic – comparison to MODIS and CALIPSO. *Atmos Chem Phys* 2010;10:1953–67.
- [27] Maddy ES, DeSouza-Machado SG, Nalli NR, Barnet CD, L Strow L, Wolf WW, et al. On the effect of dust aerosols on AIRS and IASI operational level 2 products. *Geophys Res Lett* 2012;39.
- [28] Clarisse L, Prata F, Lacour J-L, Hurtmans D, Clerbaux C, Coheur P-F. A correlation method for volcanic ash detection using hyperspectral infrared measurements. *Geophys Res Lett* 2010;37.
- [29] Peyridieu S, Chédin A, Capelle V, Tsamalis C, Pierangelo C, Armante R, et al. Characterisation of dust aerosols in the infrared from IASI and comparison with PARASOL, MODIS, MISR, CALIOP, and AERONET observations. *Atmos Chem Phys* 2013;13:6065–82.
- [30] Kokhanovsky AA, Leeuw Gd. *Satellite Aerosol Remote Sensing over Land*. Chichester: Praxis Publishing Ltd; 2009.
- [31] Clarisse L, Coheur PF, Prata F, Hadji-Lazarou J, Hurtmans D, Clerbaux C. A unified approach to infrared aerosol remote sensing and type specification. *Atmos Chem Phys* 2013;13:2195–221.
- [32] Leitch JW, Delker T, Good W, Ruppert L, Murcay F, Chance K, et al. The GeoTASO airborne spectrometer project. *Proc. SPIE 9218, Earth Observing Systems XIX*; 2014. p. 92181H1-9.
- [33] Bak J, Kim JH, Liu X, Chance K, Kim J. Evaluation of ozone profile and tropospheric ozone retrievals from GEMS and OMI spectra. *Atmos Meas Tech* 2013;6:239–49.
- [34] Donlon C, Berruti B, Buongiorno A, Ferreira MH, Féménias P, Frerick J, et al. The Global Monitoring for Environment and Security (GMES) Sentinel-3 mission. *Remote Sens Environ* 2012;120:37–57.
- [35] Vandembussche S, Kochenova S, Vandaele AC, Kumps N, De Mazière M. Retrieval of desert dust aerosol vertical profiles from IASI measurements in the TIR atmospheric window. *Atmos Meas Tech* 2013;6:2577–91.
- [36] Minu S, Amba S. Atmospheric correction algorithms for hyperspectral imageries: a review. *Int Res J Earth Sci* 2015;3:14–8.
- [37] Vermote EF, Saleous NZE, Justice CO. Atmospheric correction of MODIS data in the visible to middle infrared: first results. *Remote Sens Environ* 2002;83:97–111.
- [38] Vermote EF, Tanre D, Deuze JL, Herman M, Morcrette J-J. Second simulation of the satellite signal in the solar spectrum, 6S: an overview. *IEEE Trans Geosci Remote* 1997;35:675–86.
- [39] Kneizys FX, Abreu LW, Anderson GP, Chetwynd JH, Shettle EP, Berk A, et al. The MODTRAN 2/3 report and LOWTRAN 7 model (MODTRAN Report), MA, US: Ontar Corporation; 1996.
- [40] Gao B-C, Heidebrecht KB, Goetz AFH. Derivation of scaled surface reflectances from AVIRIS data. *Remote Sens Environ* 1993;44:165–78.
- [41] Richter R. A spatially adaptive fast atmosphere correction algorithm. *Int J Remote Sens* 1996;11:159–66.
- [42] Adler-Golden SM, Berk A, Bernstein LS, Richtsmeier S, Acharya PK, Matthew MW, et al. Flaash, a Modtran4 atmospheric correction package for hyperspectral data retrievals and simulations (jpl airborne earth science workshop). Pasadena, California: JPL Publication; 9–14.
- [43] Cooley T, Anderson GP, Felde GW, Hoke ML, Ratkowski AJ, Chetwynd JH, et al. FLAASH, a MODTRAN4-based atmospheric correction algorithm, its application and validation. Toronto: IGARSS; 1414–8.
- [44] ACORN 4.0, User's Guide. Boulder, US: Analytical Imaging and Geophysics, LLC; 2002.
- [45] Qu Z, Kindel BC, Goetz AFH. The high accuracy atmospheric correction for hyperspectral data (HATCH) model. *IEEE Trans Geosci Remote* 2003;41:1223–31.
- [46] Gao B-C, Kaufman YJ. Water vapor retrievals using Moderate Resolution Imaging Spectroradiometer (MODIS) near-infrared channels. *J Geophys Res Atmos* 2003;108.
- [47] Griffin MK, Burke H-hK. Compensation of hyperspectral data for atmospheric effects. *Linc Lab J* 2003;14:29–54.
- [48] Kaufman YJ, Tanré D, Gordon HR, Nakajima T, Lenoble J, Fouin R, et al. Passive remote sensing of tropospheric aerosol and atmospheric correction for the aerosol effect. *J Geophys Res Atmos* 1997;102:16815–30.

- [49] Jolliffe IT. Principal component analysis. second ed. New York, US: Springer-Verlag; 2002.
- [50] Tsai F, Lin EK, Yoshino K. Spectrally segmented principal component analysis of hyperspectral imagery for mapping invasive plant species. *Int J Remote Sens* 2007;28:1023–39.
- [51] Koutsias N, Mallinis G, Karteris M. A forward/backward principal component analysis of Landsat-7 ETM+ data to enhance the spectral signal of burnt surfaces. *ISPRS J Photogramm* 2009;64:37–46.
- [52] Rinnen S, Stroth C, Riße A, Ostertag-Henning C, Arlinghaus HF. Characterization and identification of minerals in rocks by ToF-SIMS and principal component analysis. *Appl Surf Sci* 2015;349:622–8.
- [53] Roberts YL, Pilewskie P, Kindel BC. Evaluating the observed variability in hyperspectral Earth-reflected solar radiance. *J Geophys Res Atmos* 2011;116.
- [54] Roberts YL, Pilewskie P, Kindel BC, Feldman DR, Collins WD. Quantitative comparison of the variability in observed and simulated shortwave reflectance. *Atmos Chem Phys* 2013;13:3133–47.
- [55] Aires F. Remote sensing from the infrared atmospheric sounding interferometer instrument 2. Simultaneous retrieval of temperature, water vapor, and ozone atmospheric profiles. *J Geophys Res* 2002;107.
- [56] Aires F, Rossow WB, Scott NA, Chédin A. Remote sensing from the infrared atmospheric sounding interferometer instrument 1. Compression, denoising, and first-guess retrieval algorithms. *J Geophys Res Atmos* 2002;107.
- [57] Liu X, Smith WL, Zhou DK, Larar A. Principal component-based radiative transfer model for hyperspectral sensors: theoretical concept. *Appl Opt* 2006;45:201–9.
- [58] Liu X, Zhou DK, Larar A, Smith WL, Mango SA. Case-study of a principal-component-based radiative transfer forward model and retrieval algorithm using EAQUATE data. *Q J R Meteor Soc* 2007;133:243–56.
- [59] Agahian F, Amirshahi SA, Amirshahi SH. Reconstruction of reflectance spectra using weighted principal component analysis. *Color Res Appl* 2008;33:360–71.
- [60] Bell IE, Baranoski GVG. Reducing the dimensionality of plant spectral databases. *IEEE Trans Geosci Remote* 2004;42:570–6.
- [61] Rodgers CD. Inverse methods for atmospheric sounding: theory and practice. Singapore: World Scientific; 2000.
- [62] Waquet F, Cairns B, Knobelspiesse K, Chowdhary J, Travis LD, Schmid B, et al. Polarimetric remote sensing of aerosols over land. *J Geophys Res* 2009;114.
- [63] Strahler AH, Lucht W, Schaaf CB, Tsang T, Gao F, Li X, et al. MODIS BRDF/Albedo Product: Algorithm Theoretical Basis Document Version 5.0. 1997.
- [64] Baldridge AM, Hook SJ, Grove CI, Rivera G. The ASTER spectral library version 2.0. *Remote Sens Environ* 2009;113:711–5.
- [65] Clark RN, Swayze GA, Wise R, Livo E, Hoefen T, Kokaly R, et al. USGS digital spectral library splib06a: U.S. Geological Survey, Digital Data Series 231. (<http://speclab.cr.usgs.gov/spectral.lib06>). 2007.
- [66] Wang J, Xu X, Ding S, Zeng J, Spurr R, Liu X, et al. A numerical testbed for remote sensing of aerosols, and its demonstration for evaluating retrieval synergy from a geostationary satellite constellation of GEO-CAPE and GOES-R. *J Quant Spectrosc Radiat Transf* 2014;146:510–28.
- [67] Xu X, Wang J. Retrieval of aerosol microphysical properties from AERONET photopolarimetric measurements: 1. Information content analysis. *J Geophys Res Atmos* 2015;120:7059–78.
- [68] Xu X, Wang J, Zeng J, Spurr R, Liu X, Dubovik O, et al. Retrieval of aerosol microphysical properties from AERONET photopolarimetric measurements: 2. A new research algorithm and case demonstration. *J Geophys Res Atmos* 2015;120:7079–98.
- [69] Spurr RJD. VLIDORT: a linearized pseudo-spherical vector discrete ordinate radiative transfer code for forward model and retrieval studies in multilayer multiple scattering media. *J Quant Spectrosc Radiat Transf* 2006;102:316–42.
- [70] Spurr R, Wang J, Zeng J, Mishchenko MI. Linearized T-matrix and Mie scattering computations. *J Quant Spectrosc Radiat Transf* 2012;113:425–39.
- [71] Lyapustin A, Wang Y, Laszlo I, Kahn R, Korokin S, Remer L, et al. Multiangle implementation of atmospheric correction (MAIAC): 2. Aerosol algorithm. *J Geophys Res Atmos* 2011;116.
- [72] Dozier J, Painter TH. Multispectral and hyperspectral remote sensing of alpine snow properties. *Annu Rev Earth Planet Sci* 2004;32:465–94.
- [73] Martynenko D, Holzer-Popp T, Elbern H, Schroedter-Homscheidt M. Understanding the aerosol information content in multi-spectral reflectance measurements using a synergetic retrieval algorithm. *Atmos Meas Tech* 2010;3:1589–98.
- [74] Babaei V, Amirshahi SH, Agahian F. Using weighted pseudo-inverse method for reconstruction of reflectance spectra and analyzing the dataset in terms of normality. *Color Res Appl* 2011;36:295–305.
- [75] Campbell SL, Meyer CDJ. Generalized inverses of linear transformations. New York: Dover; 1991.
- [76] Roujean J-L, Leroy M, Deschamps P-Y. A bidirectional reflectance model of the Earth's surface for the correction of remote sensing data. *J Geophys Res Atmos* 1992;97:20455–68.
- [77] Wanner W, Li X, Strahler AH. On the derivation of kernels for kernel-driven models of bidirectional reflectance. *J Geophys Res Atmos* 1995;100:21077–89.
- [78] Litvinov P, Hasekamp O, Cairns B. Models for surface reflection of radiance and polarized radiance: Comparison with airborne multi-angle photopolarimetric measurements and implications for modeling top-of-atmosphere measurements. *Remote Sens Environ* 2011;115:781–92.
- [79] Dubovik O, King MD. A flexible inversion algorithm for retrieval of aerosol optical properties from Sun and sky radiance measurements. *J Geophys Res Atmos* 2000;105:20673–96.
- [80] Luenberger DG, Ye Y. Linear and Nonlinear Programming, third ed., 2008, Stanford: Springer.
- [81] Byrd RH, Lu P, Nocedal J, Zhu C. A limited memory algorithm for bound constrained optimization. Evanston: Northwestern University; 1994.
- [82] Zhu C, Byrd RH, Lu P, Nocedal J. L-BFGS-B-Fortran subroutines for large-scale bound constrained optimization. Evanston: Northwestern University; 1994.
- [83] Hess M, Koepke P, Schult I. Optical properties of aerosols and clouds: the software package OPAC. *Bull Am Meteorol Soc* 1998;79:831–44.
- [84] Patterson EM, Gillette DA, Stockton BH. Complex index of refraction between 300 and 700 nm for Saharan aerosols. *J Geophys Res* 1977;82:3153–60.
- [85] Wagner R, Ajtai T, Kandler K, Lieke K, Linke C, Müller T, et al. Complex refractive indices of Saharan dust samples at visible and near UV wavelengths: a laboratory study. *Atmos Chem Phys* 2012;12:2491–512.
- [86] Wang J, Christopher SA, Brechtel F, Kim J, Schmid B, Redemann J, et al. Geostationary satellite retrievals of aerosol optical thickness during ACE-Asia. *J Geophys Res Atmos* 2003;108.
- [87] Wang J, Christopher SA, Reid JS, Maring H, Savoie D, Holben BN, et al. GOES 8 retrieval of dust aerosol optical thickness over the Atlantic Ocean during PRIDE. *J Geophys Res Atmos* 2003;108.
- [88] Zhang J, Christopher SA, Holben BN. Intercomparison of smoke aerosol optical thickness derived from GOES 8 imager and ground-based Sun photometers. *J Geophys Res Atmos* 2001;106:7387–97.
- [89] Knapp KR, Frouin R, Kondragunta S, Prados A. Toward aerosol optical depth retrievals over land from GOES visible radiances: determining surface reflectance. *Int J Remote Sens* 2005;26:4097–116.
- [90] Wang J, Xu X, Spurr R, Wang Y, Drury E. Improved algorithm for MODIS satellite retrievals of aerosol optical thickness over land in dusty atmosphere: implications for air quality monitoring in China. *Remote Sens Environ* 2010;114:2575–83.